Wind and Structures, *Vol. 30, No. 5 (2020) 525-532*
DOI: https://doi.org/10.12989/was.2020.30.5.525

The effect of Reynolds number on the elliptical cylinder wake

Xiaoyu Shi[1a], Md. Mahbub Alam[*1], Honglei Bai[2b] and Hanfeng Wang[3c]

[1]*Institute of Turbulence-Noise-Vibration Interaction and Control, Harbin Institute of Technology (Shenzhen), Shenzhen, China*
[2]*School of Aeronautics and Astronautics, Sun Yat-sen University (Shenzhen), China*
[3]*School of Civil Engineering, Central South University, Changsha, China*

(*Received November 14, 2019, Revised January 9, 2020, Accepted January 26, 2020*)

Abstract. This work numerically investigates the effects of Reynolds number Re_D (= 100 - 150), cross-sectional aspect ratio AR = (0.25 -1.0), and attack angle α (= 0° - 90°) on the forces, Strouhal number, and wake of an elliptical cylinder, where Re_D is based on the freestream velocity and cylinder cross-section height normal to the freestream flow, AR is the ratio of the minor axis to the major axis of the elliptical cylinder, and α is the angle between the cylinder major axis and the incoming flow. At Re_D= 100, two distinct wake structures are identified, namely 'Steady wake' (pattern I) and 'Karman wake followed by a steady wake (pattern II)' when AR and α are varied in the ranges specified. When Re_D is increased to 150, an additional wake pattern, 'Karman wake followed by secondary wake (pattern III)' materializes. Pattern I is characterized by two steady bubbles forming behind the cylinder. Pattern II features Karman vortex street immediately behind the cylinder, with the vortex street transmuting to two steady shear layers downstream. Inflection angle α_i = 32°, 37.5° and 45° are identified for AR = 0.25, 0.5 and 0.75, respectively, where the wake asymmetry is the greatest. The α_i effectively distinguishes the dependence on α and AR of force and vortex shedding frequency at either Re_D. In Pattern III, the Karman street forming behind the cylinder is modified to a secondary vortex street. At a given AR and α, Re_D = 150 renders higher fluctuating lift and Strouhal number than Re_D = 100.

Keywords: elliptical cylinder; wake; secondary vortex shedding

1. Introduction

The flow past a bluff body (e.g., circular or square cylinder) attracts much attention due to its significance in engineering applications (Sohankar *et al.* 1999, Daniel and Kunihiko 2015, Alam 2016, Bai and Alam 2018, Bhatt and Alam 2018, Alam *et al.* 2016, Wang *et al.* 2017, Derakhshandeh and Alam 2019). Because of complexity in the geometry of an elliptical cylinder, less attention has been paid to the flow past an elliptical cylinder whose cross-sectional aspect ratio AR (= ratio of minor axis b to major axis a) changing from 0 to 1.0 leads to the modification of the cylinder shape from a flat plate to a circular cylinder. The structure with the elliptical section is also typical both in nature and in engineering applications. Recently, there has been a surge of interest in investigating the elliptical cylinder wake, given that a sea lion whisker (whose cross-section is elliptic) does not experience vortex-induced vibration and can easily detect preys (Dehnhardt *et al.* 2001, Glaser *et al.* 2011, Miersch *et al.* 2011, Hans *et al.* 2014, Beem and Triantafyllou 2015).

Jin *et al.* (1989) conducted a two-dimensional numerical study on an elliptical cylinder of AR = 0.15, with the attack angle α varying from 0° - 90°. The Reynolds number Re_a, based on a, was 25 - 600. They observed five flow regimes, including two steady wakes and three unsteady wakes. Johnson *et al.* (2001) further carried out two-dimensional numerical simulations of the flow around a cylinder of AR = 0.01 - 1.00 at Re_a = 30 – 200 for a fixed α = 90°. A secondary vortex shedding in the wake was identified. Afterward, the formation mechanism of the secondary wake has been an interesting topic. By analyzing temporal wake evolution, Johnson *et al.* (2004), Paul *et al.* (2016) and Pulletikurthi *et al.* (2018) found three flow regions in the wake, namely linear, transition and saturation regions. For Re_a = 75 - 175, α = 90° and AR = 0.01 - 1.00, Johnson *et al.* (2004) explored that increasing Re_a or decreasing AR led to an emergence of a secondary or tertiary frequency in the power spectra of the streamwise velocity at the wake centerline. The secondary or tertiary frequency (low-frequency unsteadiness) stems from the interaction between the two-dimensional instability of the far wake and vortex shedding from the cylinder. Paul *et al.* (2016) illuminated the low-frequency unsteadiness by means of a signal decomposition method on the velocity signal. They performed the two-dimensional simulation on elliptical cylinder varying from a flat plate (AR = 0.1) to a circular cylinder (AR = 1.0) with α=90° and Re_a < 190. They believed that the secondary frequency in the far wake comes from the transition region, and the saturation region is responsible only for the primary shedding frequency. Recently, Pulletikurthi *et al.* (2018) performed a fast Fourier transform (FFT) of velocity fields (i.e., streamwise velocity, cross-stream velocity, and velocity magnitude) and scalar

*Corresponding author, Ph.D. Professor
E-mail: alam@hit.edu.cn; alamm28@yahoo.com
[a]Ph.D. Student
[b]Ph.D. Associate Professor
[c]Ph.D. Professor

ISSN: 1226-6116 (Print), 1598-6225 (Online)

fields (i.e., pressure, temperature). Only one case (AR = 0.4, α = 90° and Re_a = 130) was considered in their study. They accounted that the spectral and physical sources of the low-frequency unsteadiness are the signal in the transition region and the chaotic behavior of the flow structure aiding in the transmutation of their wavelength, respectively.

Besides, the fluid force acting on the elliptical cylinder has also been investigated for very low or high Reynolds numbers. At a fixed AR = 0.2 and α = 0° - 90°, Dennis and Young (2003) numerically investigated the steady flow around an elliptical cylinder at $1 \le Re_a \le 40$. At α < 30°, there was no flow separation from the cylinder surface. The flow separation was, however, observed for α > 30°, generating a steady asymmetric near wake, with one recirculation region attached to the cylinder and another recirculation region detached from the cylinder. Yazdi and Khoshnevis (2018) investigated the effect of the Re_a(= 15000 - 30000) on a flow structure around an elliptic cylinder (AR = 0.5, α = 90°) in a wind tunnel. The near wake was strongly dependent on Re_a, while the Strouhal number (St) remained constant with increasing Re_a. This result is in an agreement with Ota *et al.* (1987), who considered that α had no influence on St.

The review suggests that the near wake of an elliptical cylinder is strongly dependent on α, AR and Re_a. In the literature, with Re_a keeping constant, AR and/or α were varied. In such a case, the effective Reynolds number Re_D (based on the projected dimension D normal to the flow, Fig. 1(a)) is not constant, but varied. The effective Reynolds number (i.e., Re_D) thus changes as α increases from 0° to 90°, especially at small AR. The results encompass not only the effect of α but also the effect of the Reynolds number. To extract the effect of α only, the Reynolds should be kept constant. Since the flow around a bluff body is highly sensitive to the Reynolds number particularly at low Re_D (< 10^3) (e.g., Bai and Alam 2018), it essentially needs to consider the effective Reynolds number, i.e., Re_D.

This work aims to conduct a systematic numerical study on the forces, Strouhal number and wake of an elliptical cylinder, involving a relatively wide range of α(0° - 90°) and AR(= 0.25 - 1.0). The effective Reynolds number Re_D=100 and 150 is considered. The focus is given on the flow classification and connections between the flow structures and fluid force on the cylinder for the AR and α ranges.

2. Problem definitions

The elliptical cylinder is located at the origin of the coordinate system with x- and y-axis along the streamwise and cross-stream directions, respectively (Fig. 1(b)). The aspect ratio (AR) is defined as $AR=b/a$, where a and b are the lengths of the major and minor axes, respectively. The angle of attack (α) is the angle between the major axis and the freestream flow direction. The α is varied from 0° and 90°. The projection length (perpendicular to the freestream flow) of the cylinder cross-section is defined as D. The Re_D is the effect Reynolds number based on D and freestream velocity U_∞. The flow is given from left to right, parallel to

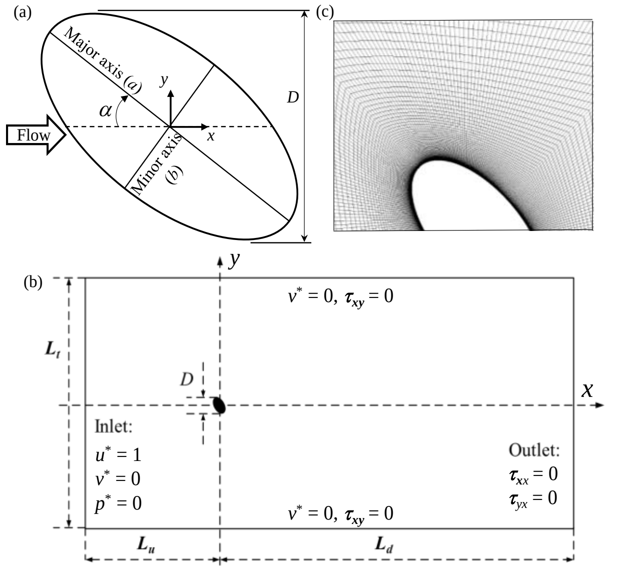

Fig. 1 (a) Cylinder model and definitions of symbols (b) Computational domain (not in scale) (c) Mesh details around the cylinder

the x-axis. The AR varies as 0.25, 0.50, 0.75 and 1.0. Given that the flow may be more sensitive at small α, a finer resolution of 5° in α was adopted for α < 30° and a coarse resolution of 15° was mulled for α > 30°. To determine the wake pattern boundary precisely, an additional α(= 37.5°) is added. Two Re_D values of 100 and 150 are considered.

2.1 Governing equations and numerical method

Two-dimensional simulations of the unsteady laminar flow around the elliptical cylinder are carried out. The incompressible continuity and Navier-Stokes (N-S) equations are solved on structural quadrilateral grids using the finite-volume method (FVM) in ANSYS Fluent. The governing equations in the dimensionless form are given below.

$$\frac{\partial \mathbf{u}^*}{\partial t^*} + (\mathbf{u}^* \cdot \nabla)\mathbf{u}^* = -\nabla p^* + \frac{1}{Re_D}\nabla^2 \mathbf{u}^* \tag{1}$$

$$\nabla \cdot \mathbf{u}^* = 0 \tag{2}$$

where t^*, $\mathbf{u}^*$ and p^* are the dimensionless time, velocity vectors (u, v), and static pressure, respectively. The superscript "*" denotes normalization based on U_∞ and/or D, unless otherwise stated.

The second-order implicit and second-order upwind differencing schemes are used for the spatial discretization of pressure and momentum, respectively. Additionally, the second-order implicit differencing scheme is applied for temporal discretization. Semi-Implicit Method for Pressure-Linked Equation (SIMPLE) is selected for the pressure-velocity coupling in the governing equation (Patankar and Spalding 1978). Statistical calculations (e.g., time-mean and root-mean-square values of the force) are made for more than 50 vortex-shedding periods after the simulation becomes statistically convergent.

2.2 Computational domain and boundary conditions

A rectangular computational domain (Fig. 1(b)) is considered, having the size of $(L_u + L_d) \times L_t = (50D + 100D) \times 100D$, where L_u is the upstream distance between the cylinder center and the inlet of the computational domain, L_d is the downstream distance between the cylinder center and the outlet of the domain, and L_t is the transverse distance between the lateral sides of the domain. The cylinder is located at the symmetric line of the computational domain. The size of the computational domain is large enough to ignore the influence the boundaries on the results.

The whole computational domain is given the structural grids. To decrease the node number and improve the computational efficiency, finer grids (Fig. 1(c)) are generated in the area of $10D \times 10D$ around the elliptical cylinder. A uniform grid spacing ($0.05D$) is applied along the cylinder surface. The number of nodes on the surface strongly depends on the *AR* and *α*. For example, for *AR* = 1.0, the number of nodes on the cylinder surface is 63, while for *AR* = 0.25, *α* = 0°, it is 300. The first grid is 0.05D away from the cylinder surface, and the grids are stretched with an expansion ratio of 1.003 along the radial direction. The total grids in the entire domain are 72K to 76K, depending on *AR* and *α*.

A constant and uniform incoming velocity (U_∞) is imposed at the inlet of the computational domain while the outflow boundary conditions ($\frac{\partial u^*}{\partial x^*} = 0$, $\frac{\partial v^*}{\partial x^*} = 0$) are used at the outlet of the domain. The symmetry boundary condition ($v^* = 0$, $\frac{\partial u^*}{\partial y^*} = 0$) is applied to the lateral sides. The no-slip boundary condition ($u^* = v^* = 0$) is set on the cylinder surface.

2.3 Grids independence tests and data validation

Before conducting the extensive simulations, the grids resolution independence tests are performed for *AR* = 1.0 (circular cylinder) at *Re* = 100. Three grid numbers are considered at first, i.e., 24K (M1), 48K (M2) and 72K (M3). The time-mean drag coefficient ($\overline{C_D}$), time-mean lift coefficient ($\overline{C_L}$), fluctuating lift force coefficient (C'_L) and Strouhal number (*St*) are extracted from the simulations and calculated as

$$\bar{C}_D = \frac{2F_x}{\rho U_\infty^2 D} \tag{3}$$

$$\bar{C}_L = \frac{2F_y}{\rho U_\infty^2 D} \tag{4}$$

$$C_L' = \frac{2F_x'}{\rho U_\infty^2 D}, \text{ and} \tag{5}$$

$$St = \frac{f_s D}{U_\infty}, \tag{6}$$

where F_x and F_y are the time-mean drag and lift forces, respectively, F'_y is the fluctuating (rms) lift force, f_S is the shedding frequency of the dominant vortices in the near wake of the cylinder, U_∞ is the free stream velocity, and ρ is the density of the fluid.

Table 1 Grid independence test results at $Re_D = 150$

Case	Mesh nodes	Δt^*	$\bar{C}_D$	C'_L	*St*
M1	24k	0.164	1.302	0.360	0.178
M2	48k	0.082	1.310	0.366	0.181
M3	72k	0.055	1.313	0.364	0.183
M3	72k	0.027	1.313	0.364	0.183

Table 2 A comparison between present and previous results for a circular cylinder at $Re_D = 150$

Research	$\bar{C}_D$	C'_L	*St*
Present	1.313	0.364	0.183
Henderson (1995), *Exp.*	1.34	—	—
Williamson (1989), *Exp.*	—	—	0.183
Zafar & Alam (2019), *Num.*	1.349	0.353	0.185
Jiang *et al.* (2016), *Num.*	1.333	0.361	0.185 (2D)
	—	—	0.184 (3D)

Table 3 A comparison between the present and published results for circular cylinder at $Re_D = 100$

Research	$\bar{C}_D$	C'_L	*St*
Present result (M3)	1.326	0.229	0.164
Jeongyoung *et al.* (1989), *Num.*	1.33	0.23	0.165
Sharman *et al.* (2005), *Num.*	1.33	0.23	0.164
Zhang and Dalton (1998), *Num.*	1.32	0.23	—
Williamson (1996) *Num.*	—	—	0.164

Table 1 lists the results of $\overline{C_D}$, C'_L, and *St* from M1, M2, and M3 for Re_D=100. The M2 and M3 provide similar results, the maximum deviation being 0.5% for C'_L. Table 1 also provides evidence that there is no difference in the results between a time step Δt^* = 0.055 and its half (= 0.027) for case M3 with the grid number 72k. Therefore, M3 is applied to extensive simulation.

Table 2 compares the present and published results in the literature. The maximum differences between the present $\overline{C_D}$, C'_L, and *St* and those in the literature are 2.1%, 0.8%, and 1.1%, respectively, providing confidence that this mesh resolution is high enough.

A similar mesh system is applied at Re_D = 100. The output is again validated for the circular cylinder. Table 3 lists the present and previous results. The maximum deviations of the present $\overline{C_D}$, C'_L and *St* from those in the literature are 0.45%, 0.43%, and 0.6%, respectively, which further proves that the mesh resolution is large enough and is adapted to conduct the extensive simulation.

3. Dependence of flow on *AR* and *α* at Re_D=100

3.1 Flow structures

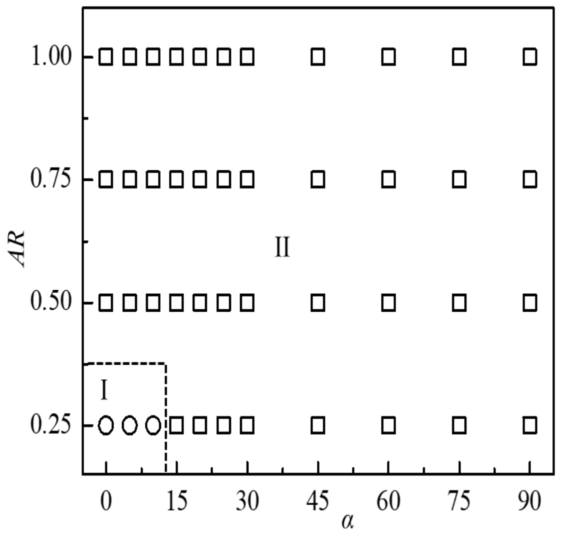

Fig. 2 Dependence of flow patterns on AR and α. ○, pattern I: steady wake; □, pattern II: Karman wake followed by steady wake. The dashed lines represent the boundaries between the patterns. Re_D = 100

At Re_D = 100, two distinct wake patterns are identified based on the flow structure and force distributions when AR is varied from 0.25 to 1.0 and α from 0° to 90°. They are named 'steady wake' (pattern I) and 'Karman wake followed by a steady wake' (pattern II). The dependence of the flow patterns on AR and α is summarized in Fig. 2. As indicated by the dashed lines, the boundary between the flow patterns is determined as the mid of the concerned points. Pattern I appears at AR < 0.375 and α < 12.5° while pattern II covers the rest of AR and α domain.

Fig. 3(a) and 3(b) shows instantaneous vorticity contours for pattern I (AR = 0.25, α = 0 º) and pattern II (AR=0.25, α=90 º), respectively. The streamwise velocities (u^*) at (x^*, y^*) = (10, 0) and (80, 0) for the two flow patterns are presented to show whether the wake is steady (Fig. 3(c) and 3(d). For pattern I (steady wake), two steady shear layers form downstream (Fig. 3(a)). The corresponding u^* at each of the two locations is constant, indicating a steady wake. For pattern II (Karman wake followed by a steady wake), the Karman vortex appears immediately downstream of the cylinder and then transits to two steady shear layers (Fig. 3(b)). The u^* signal at (x^*, y^*) = (10, 0) displays periodic fluctuations, while it is invariant at (x^*, y^*) = (80, 0), suggesting the wake back to a steady state.

The power spectral analysis is performed of the lift coefficient (C_L) and the cross-stream velocity (v^*) at (x^*, y^*) = (5, 0), where the Karman wake occurs, for pattern II (AR = 0.25, α = 90 º) and the results are presented in Fig. 4. The predominant peaks in the spectra for C_L and v^* have the same value f_1^* = 0.179, which is the vortex shedding frequency from the cylinder. The third harmonic peaks are detected in the spectra for both signals.

3.2 Force distributions

Variations in fluid forces ($\overline{C_D}$, $\overline{C_L}$, C'_L) with α for each AR are presented in Fig. 5. The horizontal dashed lines indicate the values for AR=1.0 (circular cylinder). At AR = 0.25 and α < 12.5° (pattern I), $\overline{C_D}$ is the smallest, more or less constant, about 25% smaller than $\overline{C_{D0}}$ (circular cylinder, AR=1.00). For the same AR with α > 12.5° (pattern II), $\overline{C_D}$ grows with α, reaching a maximum of 2.1 at α = 90°. The same happens for the other AR (pattern II), $\overline{C_D}$ increasing with α. The angle corresponding to $\overline{C_D}$ = $\overline{C_{D0}}$ is distinct for different AR. We define this angle as the inflection (zero curvature) angle α_i = 32°, 37.5° and 45° for AR = 0.25, 0.5 and 0.75, respectively. Interestingly, the rate of $\overline{C_D}$ increase (i.e., $\partial^2\overline{C}_D/\partial^2\alpha$, curvature) is positive at α < α_i and negative at α > α_i. At a small α (< 25°), $\overline{C_{D0}}$ enhances with increasing AR, while the opposite relationship persists at a large α (> 37.5°), $\overline{C_D}$ waning with AR.

The dependence of $\overline{C_L}$ on α is different from that of $\overline{C_D}$. The $\overline{C_L}$ for a given AR initially increases with α, reaching a maximum, followed by a declination with a further increase in α. The α_i links to the maximum $\overline{C_L}$ (i.e., $\overline{C_L}$,max) for AR=0.5 and 0.75, while close to $\overline{C_L}$,max for AR= 0.25. The value of $\overline{C_L}$ signifies a degree of asymmetry in the wake. That is, the asymmetry of the wake is the largest at α=α_i. The C'_L for pattern I is zero due to the steady wake. Naturally, $\overline{C_L}$ = 0 = $\overline{C_{L0}}$, for AR = 1.00, irrespective of α. A decrease in AR from 1.00 leads to an increase in $\overline{C_L}$ for 0º < α < 90º. While C'_L increases with increasing α from 0º to 90º for AR = 0.5 and 0.75, it decreases with increasing α at α > 60° for AR = 0.25. The α_i again corresponds to a zero curvature in C'_L distributions, with C'_L = C'_{L0} at α_i.

4. Reynolds number effects

The Reynolds number, particularly when low, dramatically affects the flow around a bluff body (Bai and Alam 2018). Here, the flow map for Re_D = 150 is presented in Fig. 6 that can be compared to Fig. 2 to assimilate the Reynolds number effect on the wake of the cylinder. One intriguing effect of Re_D is that at Re_D = 150 an additional flow pattern III (Karman wake followed by a secondary wake) appears at high α (> 52° – 82°) and small AR (≤ 0.37 – 0.67) (Fig. 6), where the Karman wake produced immediately downstream of the cylinder transmutes into a secondary wake with a low frequency, through generation of two elongated shear layers between the Karman and secondary wakes (Fig. 6(b)). Another Re_D effect is that the region of pattern I shrinks in the α domain (α < 2.5°) at Re_D = 150, compared to that (α < 12.5°) at Re_D = 100.

A comparison of the forces ($\overline{C_D}$, $\overline{C_L}$ and C'_L) between Re_D = 100 (upper row) and 150 (lower row) is shown in Fig. 7, with the flow maps superimposed on AR - α plane. The dashed lines mark the boundaries between flow patterns while the dotted-dash line represents α = α_i. The minimum and maximum values in color bars are the corresponding minimum and maximum values at Re_D = 150. The symbol '★' in color bar indicates the value for AR = 1.0 (circular cylinder).

The dependences of $\overline{C_D}$ on AR and α at the two

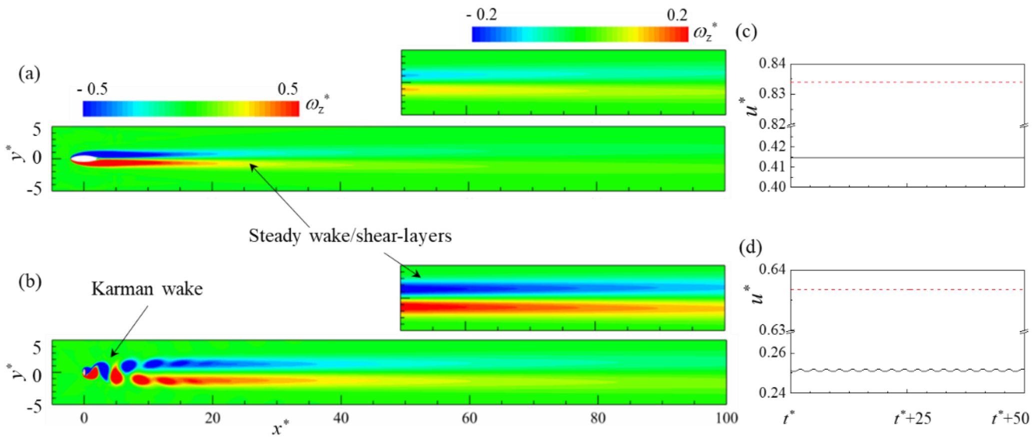

Fig. 3 Instantaneous vorticity contours for (a) pattern I: steady wake (AR = 0.25, α = 0°) and (b) pattern II: Karman wake followed by the steady wake (AR = 0.25, α = 90°). Insets are the zoom-in views of the vorticity contours (color code rescaled) for x^* = 50 - 100. (c, d) Time histories of streamwise velocity (u^*) at (x^*, y^*) = (10, 0) (solid black line) and (80, 0) (dashed red line) corresponding to (a, b), respectively

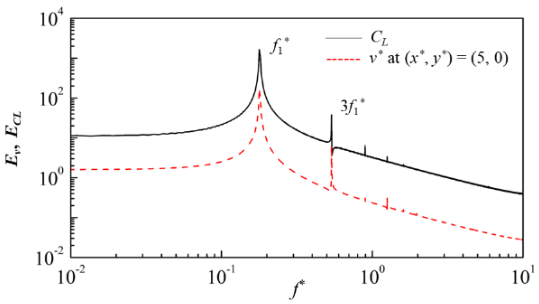

Fig. 4 Power spectra density functions of C_L and v^* at (x^*, y^*) = (5, 0) for pattern II (AR = 0. 25, α = 90°). Re_D = 100

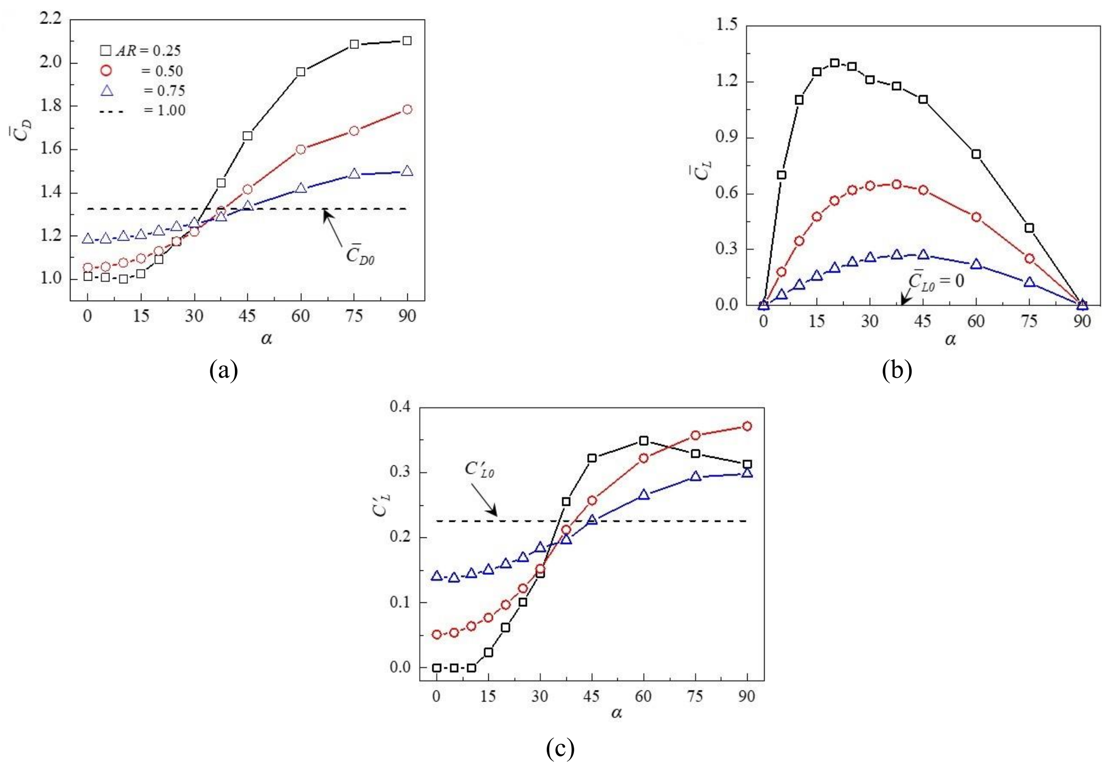

Fig. 5 Variations in (a) time-mean drag coefficient $\bar{C}_D$, (b) time-mean lift coefficient $\bar{C}_L$, and (c) fluctuating lift coefficient (C'_L) with α for different AR. Re_D = 100

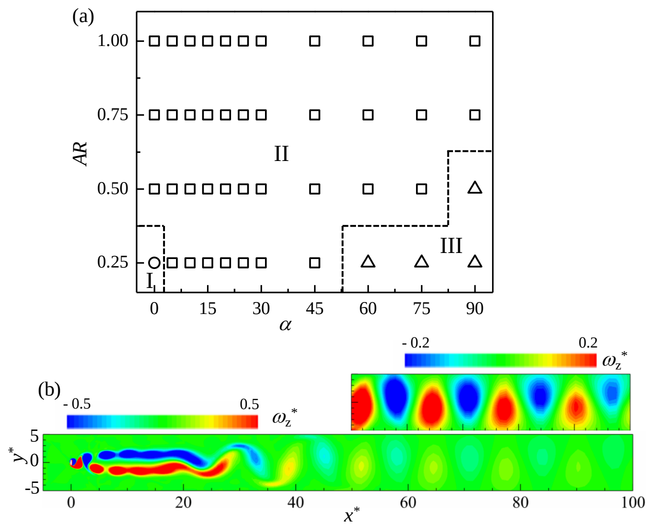

Fig. 6 (a) Dependence of flow patterns on AR and α. ○, pattern I: steady wake; □, pattern II: Karman wake followed by steady wake; △, pattern III: Karman wake followed by secondary wake. The dashed lines represent the boundaries between different patterns. (b) Instantaneous vorticity contours for pattern III (AR = 0.25, α = 90°). Re_D = 150

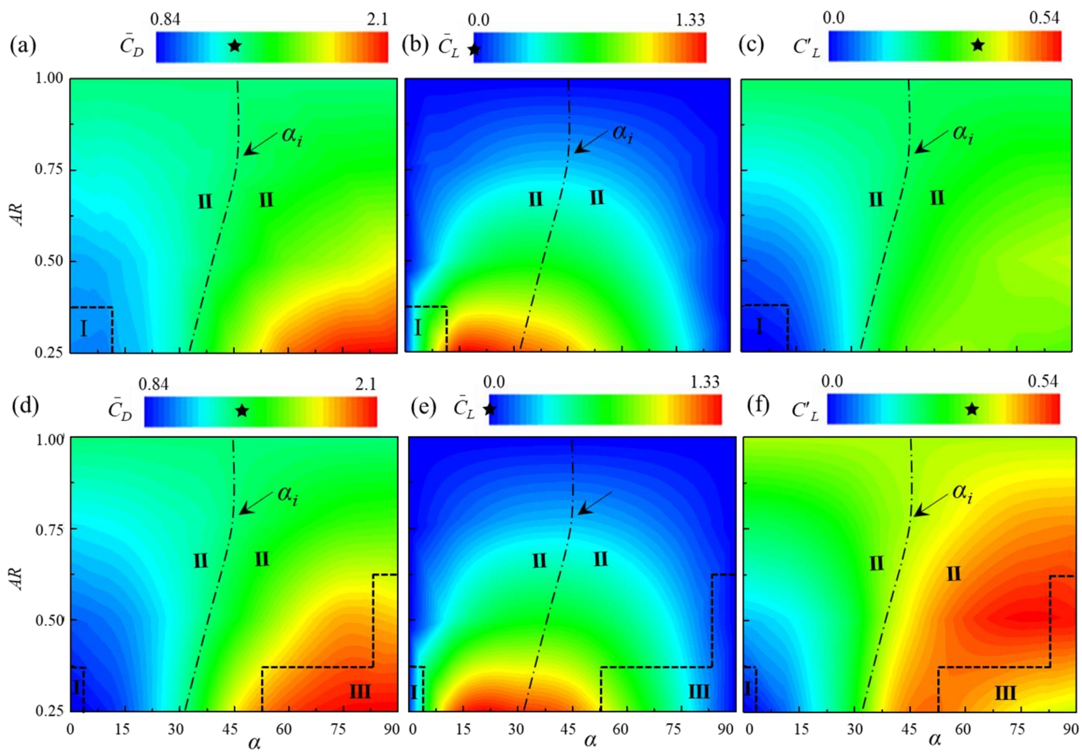

Fig. 7 Comparison of forces between Re=100 and 150. (a - c) $\bar{C}_D$, $\bar{C}_L$ and C'_L at Re_D =100. (d - f) $\bar{C}_D$, $\bar{C}_L$ and C'_L at Re_D= 150. Dashed lines mark the flow patterns while the dotted-dash line represent $\alpha = \alpha_i$. In the color code bars, the minimum and maximum values corresponding to the minimum and maximum values at Re_D= 150. The symbol '★' indicates the value for AR = 1.0 (circular cylinder).

Reynolds numbers are qualitatively similar to each other. Compared to those at Re_D = 100, the maximum and minimum magnitudes at Re_D = 150 are however large and small, respectively, perceived from the intensity of color. Although pattern III does not emerge at Re_D = 100, the maximum $\overline{C_D}$ regime still locates at a similar region for both Reynolds numbers. The $\overline{C_D}$ is highly sensitive to both AR and α, particularly at AR < 0.75, while Re_D largely affects the maximum and minimum magnitudes of $\overline{C_D}$. At a given α, the $\overline{C_D}$ upturns with increasing AR. The influence of α on $\overline{C_D}$ is nevertheless not straight forward, $\overline{C_D}$ diminishing and growing with AR for $\alpha < \alpha_i$ and $\alpha > \alpha_i$, respectively.

The $\overline{C_L}$= 0 on the lines α = 0° and 90° and AR = 1.00

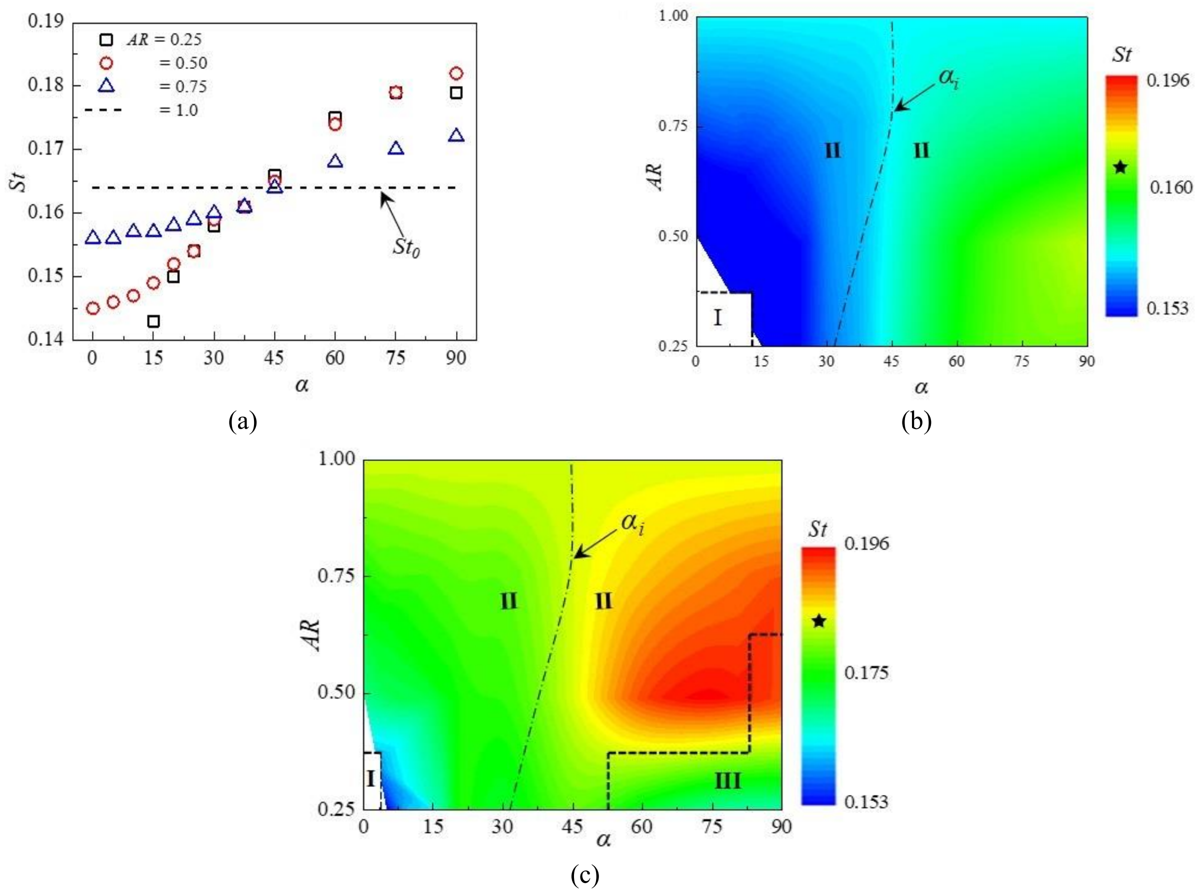

Fig. 8. (a) Dependence of *St* on α and *AR* at $Re_D = 100$. (b, c) Contours of *St* in α - *AR* plane at $Re_D = 100$ and 150, respectively. In the color code bar, the minimum and maximum values corresponding to the minimum and maximum values at $Re_D = 150$. The symbol '★' indicates the value for *AR* = 1.0 (circular cylinder)

(i.e., left, right and upper boundaries) at either Re_D. At given α, the maximum $\overline{C_L}$ roughly corresponds to $\alpha = \alpha_i$. The magnitude of $\overline{C_L}$ does not change much between the two Reynolds numbers (Fig. 7(b) and 7(e)) whilst that of C'_L significantly increases from $Re_D = 100$ to 150 (Fig. 7(c) and 7(f)).

As expected, C'_L is zero for pattern I (steady wake), and it strengthens with the increasing *AR* and α. The maximum C'_L materializes at *AR*=0.50, α = 75° - 90° for both Reynolds numbers.

Strouhal number distributions as a function of α for different *AR* are shown in Fig. 8(a). The *St* enhances with increasing α, the enhancement being rapid for *AR* = 0.25. Regardless of *AR*, $St \approx St_0$ at α = 45°. The contour plots of *St* in α-*AR* plane at $Re_D = 100$ and 150 are given in Fig. 8(b) and 8(c), respectively. Though the nature of the distributions is qualitatively the same for the two Reynolds numbers, $Re_D = 150$ complements a higher *St* than $Re_D = 100$ in the entire domain.

5. Conclusions

A numerical investigation is conducted on the effects of *AR* (= 0.25 - 1.0), α (= 0° - 90°), and Re_D (=100 and 150) on the cylinder wake, flow classification, forces and *St*. Base on the flow structure evolution in the wake, two flow patterns are identified at $Re_D = 100$, namely 'steady wake (pattern I)' and 'Karman wake followed by a steady wake (pattern II)'. As Re_D is increased to 150, pattern III (Karman wake followed by a secondary wake) emerges for large α and small *AR*. While pattern I is characterized by a steady wake, pattern II features the Karman wake immediately behind the cylinder, with the Karman wake transmuting to a steady wake downstream. For pattern III, a secondary unsteady wake is generated downstream of the Karman wake. An inflection angle α_i is marked for each *AR*, where $\overline{C_D}$, = $\overline{C_{D0}}$, , $\overline{C_L}$, ≈ $\overline{C_L}$,max and $C'_L = C'_{L0}$, with α_i = 32°, 37.5° and 45° for *AR*=0.25, 0.5 and 0.75, respectively.

Though a qualitatively similar dependence of $\overline{C_D}$, $\overline{C_L}$, and C'_L on *AR* and α is observed at both Reynolds numbers, the maximum and minimum magnitudes are however bigger and smaller, respectively, at $Re_D = 150$ than at $Re_D = 100$. The $\overline{C_D}$, $\overline{C_L}$, and C'_L all are highly dependent on both *AR* (< 0.75) and α (= 0° - 90°). The $\overline{C_D}$, and C'_L both increases with increasing *AR*, while waning with increasing *AR* for $\alpha < \alpha_i$ and boosting for $\alpha > \alpha_i$. The maximum $\overline{C_L}$, roughly corresponds to $\alpha = \alpha_i$. The magnitude of C'_L significantly enhances from Re_D = 100 to 150. The C'_L becomes maximum at *AR* = 0.50, α = 75° - 90° for both

Reynolds numbers. The $St < St_0$ and $St > St_0$ at $\alpha < 45°$ and $\alpha > 45°$, respectively. For a given *AR* and α, the *St* is higher at $Re_D = 150$ than at $Re_D = 100$.

Acknowledgments

The authors wish to acknowledge the support given by the National Natural Science Foundation of China through Grants 11672096, 91752112 and 11872018 and by Research Grant Council of Shenzhen Government through grant JCYJ20180306171921088.

References

Alam, M.M. (2016), “Lift forces induced by phase lag between the vortex sheddings from two tandem bluff bodies”, *J. Fluid Struct*., **65**, 217-237. https://doi.org/10.1016/j.jfluidstructs.2016.05.008.

Alam, M.M., Bai, H.L. and Zhou, Y. (2016), “The wake of two staggered square cylinders”, *J. Fluid Mech*., **801**, 475-507. https://doi.org/10.1017/jfm.2016.303

Bai, H.L. and Alam, M.M. (2018), “Dependence of square cylinder wake on Reynolds number”, *Phys. Fluid*, **30**(1), 015102. https://doi.org/10.1063/1.4996945.

Beem, H.R. and Triantafyllou, M.S. (2015), “Wake-induced ‘slaloming’ response explains exquisite sensitivity of seal whisker-like sensors”, *J. Fluid Mech*., **783**, 306-322. https://doi.org/10.1017/jfm.2016.303

Bhatt, R. and Alam, M.M. (2018), “Vibrations of a square cylinder submerged in a wake”. *J. Fluid Mech.*, **853**, 301-332. https://doi.org/10.1017/jfm.2018.573.

Daniel, C. and Kunihiko, T. (2015), “Two-dimensional compressible viscous flow around a circular cylinder”, *J. Fluid Mech*., **785**, 349-337. https://doi.org/10.1017/jfm.2015.635.

Derakhshandeh, J.F. and Alam, M.M. (2019), “A review of bluff body wakes”, *Ocean Eng*., **182**, 475-488.

Dehnhardt, G., Mauck, B., Hanke, W. and Bleckmann, H. (2001), “Hydrodynamic trail-following in harbor seals (Phoca vitulina)”, *Science*, **293**(5527), https://doi.org/102-104. 10.1126/science.1060514.

Dennis, S.C.R. and Young, P.J.S. (2003), “Steady flow past an elliptic cylinder inclined to the stream”, *J. Eng. Math*., **47**, 101-120. https://doi.org/10.1023/A:1025872419183.

Glaser, N., Wieskotten, S., Otter, C., Dehnhardt, G., and Hanke, W. (2011), “Hydrodynamic trail following in a California sea lion (Zalophus californianus)”, *J. Comparative Physiol. A*, **197**(2), https://doi.org/141-151. 10.1007/s00359-010-0594-5.

Hans, H., Miao, J.M., and Triantafyllou, M.S. (2014), “Mechanical characteristics of harbor seal (Phoca vitulina) vibrissae under different circumstances and their implications on its sensing methodology”, *Bioinspir Biomim*, **9**(3), 036013. https://doi.org/10.1088/1748-3182/9/3/036013.

Henderson, R.D. (1995), “Detail of the drag curve near the onset of vortex shedding using high-resolution computer simulation”, *Phys. Fluids*, **7**(9), 2102-2104. https://doi.org/10.1063/1.868459.

Jeongyoung, P., Kiyoung, K. and Haecheon, C. (1989), “Numerical solutions of flow past a circular cylinder at Reynolds numbers up to 160”, *J. Mech. Sci. Technol*., **12**(6), 1200-1205. https://doi.org/10.1007/bf02942594.

Jiang, H., Cheng, L., Draper, S., An, H. and Tong, F. (2016), “Three-dimensional direct numerical simulation of wake transitions of a circular cylinder”, *J. Fluid Mech*., **801**, 353-391. https://doi.org/10.1017/jfm.2016.446.

Jin, K.P., Seung, O.P. and Hyun, J.M. (1989), “Flow regimes of unsteady laminar flow past a slender elliptic cylinder at incidence”. *Int. J. Heat Fluid Flow*, https://doi.org/10.1016/0142-727x(89)90019-2.

Johnson, S.A., Thompson, M.C. and Hourigan, K. (2001), “Flow Past Elliptical Cylinders at Low Reynolds Numbers”, *In Proc. 14th Australasian Fluid Mechanics Conference*, Adelaide University, Australia, December.

Johnson, S.A., Thompson, M.C. and Hourigan, K. (2004), “Predicted low frequency structures in the wake of elliptical cylinders”, *European J. Mech. - B/Fluids*, **23**(1), 229-239. https://doi.org/10.1016/j.euromechflu.2003.05.006.

Miersch, L., Hanke, W., Wieskotten, S., Hanke, F.D., Oeffner, J., Leder, A. and Dehnhardt, G. (2011), “Flow sensing by pinniped whiskers”, *Philosophical Transactions of the Royal Society B: Biological Sciences*, **366**(1581), 3077-3084. https://doi.org/10.1098/rstb.2011.0155.

Ota, T., Nishiyama, H. and Taoka, Y. (1987), “Flow around an elliptic cylinder in the critical Reynolds number regime”, J. Fluids Eng., **109**(2), 149-155. https://doi.org/10.1115/1.3242635.

Patankar, S.V. and Spalding, D.B. (1978), “Computer analysis of the three-dimensional flow and heat transfer in a steam generator”, *Forschung Im Ingenieurwesen*, **44**(2), 47-52. https://doi.org/10.1007/BF02560744.

Paul, I., Prakash, K.A., Vengadesan, S. and Pulletikurthi, V. (2016), “Analysis and characterisation of momentum and thermal wakes of elliptic cylinders”, *J. Fluid Mech*., **807**, 303-323. https://doi.org/10.1017/jfm.2016.625.

Pulletikurthi, V., Paul, I., Prakash, K.A. and Prasad, B.V.S.S.S. (2018), “Spectral analysis of flow and scalar primitive variables in near and far laminar wake of an elliptic cylinder”, *arXiv preprint arXiv:1807.03417*.

Sharman, B., Lien, F.S., Davidson, L. and Norberg, C. (2005), “Numerical predictions of low Reynolds number flows over two tandem circular cylinders”, *Int. J. Numer. Meth. Fluids*, **47**(5), 423-447. https://doi.org/10.1002/fld.812.

Sohankar, A., Norberg, C. and Davidson, L. (1999), “Simulation of three-dimensional flow around a square cylinder at moderate Reynolds numbers”, *Phys. Fluids*, **11**(2), 288-306. https://doi.org/10.1063/1.869879.

Wang, L., Alam, M.M. and Zhou, Y. (2017), “Two tandem cylinders of different diameters in cross-flow: effect of an upstream cylinder on wake dynamics”, *J. Fluid Mech*., **836**, 5-42. https://doi.org/10.1017/jfm.2017.735.

Williamson, C.H.K. (1996), “Oblique and parallel modes of vortex shedding in the wake of a circular cylinder at low Reynolds numbers”, *J. Fluid Mech*., **206**(3), 579-627. https://doi.org/10.1017/S0022112089002429.

Williamson, C.H.K. (1996), “Vortex dynamics in the cylinder wake”. *Annu. Rev. Fluid Mech*., ***28***(1), 477-539. https://doi.org/10.1146/annurev.fl.28.010196.002401

Yazdi, M.J.E. and Khoshnevis, A.B. (2018), “Experimental study of the flow across an elliptic cylinder at subcritical Reynolds number”, *European Phys. J. Plus*, **133**(12). https://doi.org/10.1140/epjp/i2018-12342-1.

Zafar, F. and Alam, M.M. (2019), “Flow structure around and heat transfer from cylinders modified from square to circular”, *Phys. Fluids*, **31**, 083604.

Zhang, J. and Dalton, C. (1998), “A three-dimensional simulation of a steady approach flow past a circular cylinder at low Reynolds number”, *Int. J. Numer. Meth. Fluids*, **26**(9), 1003-1012. https://doi.org/10.1002/(sici)1097-0363(19980515)26:9<1003::aid-fld611>3.0.co;2-.

AM